

Tuning of magnetic and electronic states by control of oxygen content in lanthanum strontium cobaltites

S. Kolesnik, B. Dabrowski, J. Mais, M. Majjiga, O Chmaissem
Department of Physics, Northern Illinois University, DeKalb, IL 60115

A. Baszczuk
INTiBS, PAN, Wroclaw, Poland

J. D. Jorgensen
Materials Science Division, Argonne National Laboratory, Argonne, IL 60439
 (Dated: January 13, 2022)

We report on the magnetic, resistive, and structural studies of perovskite $\text{La}_{1/3}\text{Sr}_{2/3}\text{CoO}_{3-\delta}$. By using the relation of synthesis temperature and oxygen partial pressure to oxygen stoichiometry obtained from thermogravimetric analysis, we have synthesized a series of samples with precisely controlled $\delta = 0.00 - 0.49$. These samples show three structural phases at $\delta = 0.00 - 0.15$, ≈ 0.25 , ≈ 0.5 , and two-phase behavior for other oxygen contents. The stoichiometric material with $\delta = 0.00$ is a cubic ferromagnetic metal with the Curie temperature $T_C = 274$ K. The increase of δ to 0.15 is followed by a linear decrease of T_C to ≈ 160 K and a metal-insulator transition near the boundary of the cubic structure range. Further increase of δ results in formation of a tetragonal $2a_p \times 2a_p \times 4a_p$ phase for $\delta \approx 0.25$ and a brownmillerite phase for $\delta \approx 0.5$. At low temperatures, these are weak ferromagnetic insulators (canted antiferromagnets) with magnetic transitions at $T_m \approx 230$ and 120 K, respectively. At higher temperatures, the $2a_p \times 2a_p \times 4a_p$ phase is G -type antiferromagnetic between 230 K and ≈ 360 K. Low temperature magnetic properties of this system for $\delta < 1/3$ can be described in terms of a mixture of Co^{3+} ions in the low-spin state and Co^{4+} ions in the intermediate-spin state and a possible spin transition of Co^{3+} to the intermediate-spin state above T_C . For $\delta > 1/3$, there appears to be a combination of Co^{2+} and Co^{3+} ions, both in the high-spin state with dominating antiferromagnetic interactions.

PACS numbers: 75.30.Cr, 75.50.Cc, 81.05.Je, 81.40.Rs

I. INTRODUCTION

Strontium substituted lanthanum cobaltites with a general formula $\text{La}_{1-x}\text{Sr}_x\text{CoO}_{3-\delta}$ have attracted much interest owing to their possible applications in the field of solid oxide fuel cells^{1,2} as fast ion conducting materials and high temperature oxygen separation membranes^{3,4}. It has also been reported that substitution of Sr^{+2} in LaCoO_3 results in a remarkable change in the crystal structure^{5,6}, a metal-insulator transition,⁶ and ferromagnetic behavior.⁷ The structure of this compound with Sr substitution varying from 0 to 1 has been the subject of numerous investigations at room temperature.^{6,8,9,10} A simple cubic structure has been reported by most of the authors for samples with $x > 0.5$.^{6,8,9,10} Sunstrom et al.⁸ prepared the series of $\text{La}_{1-x}\text{Sr}_x\text{CoO}_{3-\delta}$ samples ($0.5 \leq x \leq 0.9$) using the Pechini gel technique and observed that Sr-rich samples ($x > 0.7$) take a brownmillerite structure prior to oxidation and a cubic perovskite structure after being treated with sodium hypobromite. Van Doorn and Burggraaf proposed an $a_p \times a_p \times 2a_p$ superstructure¹⁰ with distinct microdomains in $\text{La}_{0.3}\text{Sr}_{0.7}\text{CoO}_{2.82}$. A few other regions without the superstructure (normal regions) have also been identified and found to be fully oxygen-stoichiometric ($\delta = 0$), while the ones with the superstructure were found to have an oxygen content $\delta = 0.5$.

Due to mixed valence of Co ions, in addition to oxygen nonstoichiometry and fast ion conducting properties, $\text{La}_{1-x}\text{Sr}_x\text{CoO}_3$ demonstrates a rich magneto-electronic phase diagram. One end-member of this family, LaCoO_3 , is a nonmagnetic insulator with low-spin Co^{3+} ($t_{2g}^6:S = 0$) at low temperatures, which undergoes a spin-state transition at around 100 K to the intermediate-spin Co^{3+} ($t_{2g}^5e_g^1:S = 1$).¹¹ The same transition has also been reported for small Sr concentrations $x \leq 0.15$ in $\text{La}_{1-x}\text{Sr}_x\text{CoO}_3$.⁷ Low Sr substitution ($x \leq 0.30$) leads to segregation of this material into hole-rich ferromagnetic clusters in nonmagnetic matrix, similar to LaCoO_3 .⁷ Material in this doping region behaves as “cluster glass” showing both spin-glass and ferromagnetic properties.^{7,12} Increasing Sr concentration results in coalescence of the clusters and the material becomes a ferromagnetic metal for $x \geq 0.3$. With an increase of x , pronounced deviation (deficiency) from the ideal oxygen stoichiometry can be noticed for air synthesized samples. High-pressure oxygen (≈ 2600 bar) synthesis is required to obtain nearly stoichiometric material for the other end member of the family $\text{SrCoO}_{3-\delta}$ ($\delta \approx 0.05$).¹³ This material is a simple cubic perovskite metallic ferromagnet with Curie temperature $T_C = 220$ K (extrapolated to $\delta = 0$). The electrochemical oxidation method was reported to give fully stoichiometric SrCoO_3 .¹⁴ This sample is also a metallic ferromagnet with $T_C = 280$ K (determined from mea-

surements in the magnetic field of 2 T).

Our work here describes a study of the effect of oxygen non-stoichiometry on the structure and magnetic properties of the $\text{La}_{1/3}\text{Sr}_{2/3}\text{CoO}_{3-\delta}$ compound. A detailed description of the synthesis of $\text{La}_{1/3}\text{Sr}_{2/3}\text{CoO}_{3-\delta}$ with $0 \leq \delta \leq 0.49$ and precise determination of relation of oxygen content to the structure and physical properties have been made. Our results clarify discrepant reports concerning properties of $\text{La}_{1-x}\text{Sr}_x\text{CoO}_{3-\delta}$ compounds for $x > 0.5$.

II. SYNTHESIS AND EXPERIMENTAL TECHNIQUES

The conventional solid state reaction was used to prepare single-phase samples of $\text{La}_{1/3}\text{Sr}_{2/3}\text{CoO}_{3-\delta}$. Appropriate molar ratios of La_2O_3 , SrCO_3 and Co_3O_4 were mixed and repetitively finely ground and fired in air at temperatures between 800-1000°C. The sample was then pressed into pellets and fired at 1100°C. Final sintering was done at 1120°C to obtain a dense, single phase sample. In each case sample was held for 12 hours at the specified temperature. In the next stage, multiple batches of the sample each differing in the oxygen stoichiometry were obtained by additionally annealing the samples in high-pressure oxygen, argon, or air followed by quenching in liquid nitrogen. Thermogravimetric analysis was used to determine the oxygen content in each of these samples. The sample with highest oxygen content ($\delta = 0.00$) was obtained by annealing as-made sample under high-pressure oxygen (250 atm) at 500°C for several hours followed by very slow cooling to room temperature (0.1°C/min). Annealing in air under atmospheric pressure produced $\text{La}_{1/3}\text{Sr}_{2/3}\text{CoO}_{2.98}$ ($\delta = 0.02$). The sample with $\delta = 0.49$ was obtained by heating $\text{La}_{1/3}\text{Sr}_{2/3}\text{CoO}_{2.98}$ sample in pure Ar (99.9999%) at 1080°C and then quickly cooling it to room temperature. The samples with intermediate oxygen deficiencies $\delta = 0.08$ -0.33 were obtained by annealing the as-made sample ($\delta = 0.07$) in air at temperatures in the range 400-1080°C and then rapidly quenching in liquid nitrogen. The synthesis conditions and respective oxygen deficiencies are shown in Table I.

The x-ray patterns of these samples were obtained by performing x-ray diffraction at room temperature using a Rigaku Powder Diffractometer with $\text{Cu K}\alpha$ radiation. Data were collected for angles 2θ ranging from 20 to 90 degrees with a step size of 0.02 and step time of 2.4 second. Time-of-flight neutron powder diffraction data was collected at room temperature on the Special Environment Powder Diffractometer (SEPD)¹⁵ at the Intense Pulsed Neutron Source (IPNS) at Argonne National Laboratory. High-resolution backscattering data (detector bank 1, $2\theta = 144.85^\circ$) were analyzed using the Rietveld method with the GSAS (EXPGUI) suite.¹⁶ Thermogravimetric analysis with a Cahn TG 171 thermobalance was used to determine the oxygen content. These experiments were conducted at temperatures 25-1100°C in Ar,

1% O_2/Ar , 21% O_2/Ar , and pure oxygen, and provided additional samples with well-defined oxygen deficiency $\delta = 0.49$, 0.04, 0.02, and 0.01, respectively. The oxygen content was confirmed with the accuracy $\delta \pm 0.01$ by reduction of the $\delta = 0.49$ sample in 1% H_2/Ar atmosphere on the thermobalance. The material decomposes in this atmosphere to binary oxides La_2O_3 , SrO and elemental Co. A Quantum Design MPMS system equipped with a 70 kOe superconducting magnet was used to measure dc magnetization and ac susceptibility. The resistivity was measured with a Quantum Design PPMS system model 6000 using a standard four-point technique.

III. RESULTS AND DISCUSSION

A. Structural properties

Thermogravimetric measurements for various samples quenched in liquid nitrogen and fast cooled to room temperature indicate that the oxygen non-stoichiometry, δ , is strongly controlled by the atmosphere maintained during the final firing. In our experiments, we were able to obtain $\text{La}_{1/3}\text{Sr}_{2/3}\text{CoO}_{3-\delta}$ samples with δ varying from 0 to ~ 0.5 . Refinements of the diffraction patterns show that $\text{La}_{1/3}\text{Sr}_{2/3}\text{CoO}_{3-\delta}$ forms three single-phase compounds with cubic, “224” superstructure, and brownmillerite crystal structures for $\delta=0$, 0.25, and 0.49, respectively. The x-ray diffraction patterns of selected samples are shown in Fig. 1. We observe that samples with $0 \leq \delta \leq 0.15$ show single-phase x-ray diffraction patterns. These could be indexed on simple cubic ($Pm\bar{3}m$) perovskite structure. They do not show any diffraction peaks that could be attributed to the superstructure phase for this level of oxygen vacancies. The lattice parameter a obtained from Rietveld refinements varies from 3.8280(1) Å for $\delta = 0$ to 3.8389(1) Å for $\delta = 0.15$ which is the last member of the solid solution. The formal average charge of cobalt for the samples in this region decreases from 3.667 to 3.367. Splitting and broadening of the diffraction peaks (Fig. 1) was observed for samples with oxygen deficient compositions of $0.15 < \delta < 0.25$. These samples were found to contain two crystallographic phases with $\delta = 0.15$ and $\delta = 0.25$. The x-ray diffraction profile of $\text{La}_{1/3}\text{Sr}_{2/3}\text{CoO}_{2.75}$ revealed a nearly single-phase sample that could be indexed using a tetragonal $2a_p \times 2a_p \times 4a_p$ (“224”) superstructure, where a_p is the cell parameter of the cubic perovskite. However, since we were not able to observe several of the diffraction peaks unique for this superstructure, we have prepared additional large-size sample with oxygen content $\delta = 0.28$ for detailed investigation using neutron diffraction, which is described in the following subsection.

The x-ray diffraction pattern for $\text{La}_{1/3}\text{Sr}_{2/3}\text{CoO}_{2.53}$ indicate a single-phase sample. Rietveld refinement proves that sample with oxygen deficiency $\delta = 0.47$ crystallizes with the brownmillerite structure (space group $Icmm$) with alternate layers of $[\text{CoO}_6]$ octahedra and oxygen de-

TABLE I: Oxygen deficiencies, synthesis conditions, observed crystal structures, (c - cubic, 224 - $2a_p \times 2a_p \times 4a_p$ superstructure, bm - brownmillerite), reliability factors from the Rietveld refinements, and Co formal valence for $\text{La}_{1/3}\text{Sr}_{2/3}\text{CoO}_{3-\delta}$ samples. The samples were synthesized either on a thermobalance (TGA), in a regular furnace or in a high-pressure (h.p.) furnace.

Oxygen deficiency δ	Facility	Synthesis conditions			Crystal structure	Reliability factors			Cobalt formal valence
		Atmosphere	T ($^{\circ}\text{C}$)	Cooling		$R_p(\%)$	$R_{wp}(\%)$	χ^2	
0	h.p. furnace	250 bar O_2	500	slow	c	2.1	2.81	1.708	3.67
0.01	TGA	100% O_2	1100	slow	c	2.79	3.58	1.38	3.65
0.02	TGA	21% O_2/Ar	1100	slow	c	2.67	3.7	2.4	3.63
0.04	TGA	1% O_2/A	1100	slow	c	2.24	3.22	2.45	3.59
0.07	furnace	air	1120	fast	c	2.37	3.31	2.147	3.53
0.08	furnace	air	400	quench in LN_2	c	2.34	3.02	1.67	3.51
0.15	furnace	air	600	quench in LN_2	c	2.07	2.77	1.609	3.37
0.22	furnace	air	800	quench in LN_2	c+224	1.93	2.48	1.56	3.23
0.25	furnace	air	860	quench in LN_2	224	1.77	2.25	1.43	3.17
0.28	furnace	air	930	quench in LN_2	224+bm	2.3	2.89	1.36	3.11
0.33	furnace	air	1080	quench in LN_2	224+bm	1.94	2.45	1.27	3.00
0.42	furnace	Ar	900	fast	bm+224	2.63	3.39	1.96	2.83
0.47	furnace	Ar	1000	fast	bm	1.95	2.5	1.42	2.73
0.49	TGA	Ar	1100	fast	bm				2.69

efficient layers of $[\text{CoO}_4]$ tetrahedra with randomly mixed $\text{La}^{3+}/\text{Sr}^{2+}$ cations occupying the same crystallographic site. The oxygen vacancies in these $[\text{CoO}_4]$ layers were found to be ordered in such a way that they formed tetrahedra with corners linked in chains running along the $[001]$ direction.¹⁰ For the samples with $0.25 < \delta < 0.47$, two crystallographic phases are observed, namely the “224” superstructure and brownmillerite.

B. Neutron powder diffraction of $\text{La}_{1/3}\text{Sr}_{2/3}\text{CoO}_{2.72}$

The neutron powder diffraction (NPD) pattern of $\text{La}_{1/3}\text{Sr}_{2/3}\text{CoO}_{2.72}$ was successfully indexed with I -centered tetragonal unit cell related to cubic perovskite subcell by $a \approx 2a_p$ and $c \approx 4a_p$. This kind of superstructure (called in following 224) was previously reported for several A -site substituted cobalt perovskites $\text{Ln}_{1-x}\text{Sr}_x\text{CoO}_{3-\delta}$ with $x=0.67^{9,17,18,19}$ and $x=0.6^{20,21}$, where $\text{Ln} = \text{Sm-Yb}$ and Y . The origin of the superstructure was rationalized by partial Ln/Sr ordering on three crystallographic A -sites (one of them exclusively occupied by Ln and two mixed) and a presence of oxygen vacancies located solely on the O2 sites. The initial model used for the crystal structure refinement of $\text{La}_{1/3}\text{Sr}_{2/3}\text{CoO}_{2.72}$ was taken from Ref.¹⁷, with three disordered A -cation sites, two Co sites, and four oxygen sites initially set as fully occupied. The refinement revealed that oxygen vacancies were located on the O2 sites, while the O1, O3 and O4 sites were fully occupied. The refined amount of oxygen vacancies was smaller than the one determined by thermogravimetric analysis, probably because of a small fraction of brownmillerite phase (refined to $\sim 2.5\%$ wt.) present in the sample. Similar discrepancies between refined amount of oxygen and that obtained from TGA were

observed previously for $\text{Ln}_{0.33}\text{Sr}_{0.67}\text{CoO}_{3-\delta}$ compounds with $\text{Ln} = \text{Ho}$ and Y .^{18,19} In the following refinements the amount of oxygen vacancies was fixed at the TGA value. During the refinement it was found that calculated intensity of some of the diffraction peaks (in particular the 112 and 312) in the room temperature profile of $\text{La}_{1/3}\text{Sr}_{2/3}\text{CoO}_{2.72}$ were always lower than the measured intensities. The additional peak intensity could not be modelled by changes of the atomic structure, but rather, were due to magnetic Bragg scattering from ordered magnetic moments. Similar enhancement of the peak intensities was observed below antiferromagnetic transition temperature for $\text{Sr}_{0.67}\text{Y}_{0.33}\text{CoO}_{2.79}$ ¹⁸ and $\text{Sr}_{0.7}\text{Dy}_{0.3}\text{CoO}_{2.62}$ ²¹. We have tested several patterns of magnetic spin ordering for cobalt atoms and found that the best fit was observed using magnetic space group $I4/mmm'$. The magnetic refinement revealed antiferromagnetic alignment along all three crystallographic directions corresponding to G -type magnetic structure found for perovskite-type $\text{La}_{1-x}\text{Ca}_x\text{MnO}_3$ manganites²². The same G -type magnetic structure was observed recently for $\text{Ho}_{0.33}\text{Sr}_{0.67}\text{CoO}_{2.76}$ ¹⁹, $\text{Ho}_{0.1}\text{Sr}_{0.9}\text{CoO}_{2.79}$ ¹⁹, $\text{Sr}_{0.67}\text{Y}_{0.33}\text{CoO}_{2.79}$ ¹⁸, and $\text{Sr}_{0.7}\text{Dy}_{0.3}\text{CoO}_{2.62}$ ²¹ cobaltites with the 224 superstructure^{18,19,21}. The magnetic moments of cobalt atoms are directed along the c -axis. During refinement magnetic moments of Co1 and Co2 were constrained to be equal and their refined values found at $1.62(7) \mu_B$. The neutron diffraction pattern of $\text{La}_{1/3}\text{Sr}_{2/3}\text{CoO}_{2.72}$ and a difference between the measured and calculated patterns are shown in Fig. 2. Crystallographic parameters, refinement data, atomic positions, and thermal parameters are given in Table II. An examination of the bond lengths shows (Table III) that the average Co1-O bond length is 1.9237 \AA while Co2-O is considerably longer (1.9600 \AA).

Our results are similar to those found for others cobalt

TABLE II: Crystallographic parameters, atomic positions, thermal parameters, and reliability factors from the Rietveld refinements for $\text{La}_{1/3}\text{Sr}_{2/3}\text{CoO}_{2.72}$.

Atom	Site	x	y	z	B_{iso} (Å)	Occ.
Sr1/La1	8g	0	0.5	0.1384(6)	1.12(17)	0.667/ 0.333
Sr2/La2	4e	0	0	0.6335(10)	1.13(37)	0.667/ 0.333
Sr3/La3	4e	0	0	0.1271(8)	0.41(28)	0.667/ 0.333
Co1	8h	0.2442(31)	0.2442(31)	0	1.30(31)	1
Co2	8f	0.25	0.25	0.25	1.86(31)	1
O1	16m	0.2514(12)	0.2514(12)	0.1207(4)	$B_{11}=5.13(34)$ $B_{22}=5.13(34)$ $B_{33}=2.9(5)$ $B_{12}=-3.3(6)$ $B_{13}=1.0(4)$ $B_{23}=1.0(4)$	1
O2	8i	0.2632(63)	0	0	$B_{11}=-8.16(337)$ $B_{22}=-0.05(85)$ $B_{33}=-1.2(9)$ $B_{12}=0$ $B_{13}=0$ $B_{23}=0$	0.441
O3	8j	0.2787(48)	0.5	0	$B_{11}=15.16(216)$ $B_{22}=4.98(103)$ $B_{33}=1.5(9)$ $B_{12}=0$ $B_{13}=0$ $B_{23}=0$	1
O4	16n	0	0.2475(18)	0.2475(18)	$B_{11}=0.22(19)$ $B_{22}=1.84(32)$ $B_{33}=5.3(5)$ $B_{12}=0$ $B_{13}=0$ $B_{23}=-3.9(4)$	1
Space group: $I4m/m\ m$						
$a = 7.7212(21)$ Å						
$c = 15.613(4)$ Å						
$V = 930.8(7)$ Å ³						
χ^2	1.612					
R_{wp} (%)	5.68					
R_p (%)	4.24					

TABLE III: Selected interatomic distances for $\text{La}_{1/3}\text{Sr}_{2/3}\text{CoO}_{2.72}$.

Bonds	Multiplication	Distance (Å)
Co1-O1	(*2)	1.887(7)
Co1-O2	(*2)	1.893(23)
Co1-O3	(*2)	1.991(27)
<Co1-O>		1.9237
Co2-O1	(*2)	2.017(6)
Co2-O4	(*4)	1.9315(7)
<Co2-O>		1.9600
Sr1-O1	(*4)	2.7437(12)
Sr1-O2	(*2)	2.831(32)
Sr1-O3	(*2)	3.050(26)
Sr1-O4	(*2)	2.570(18)
Sr1-O4	(*2)	2.659(12)
<Sr1-O>		2.7662
Sr2-O1	(*4)	2.725(13)
Sr2-O3	(*4)	2.696(26)
Sr2-O4	(*4)	2.683(22)
<Sr2-O>		2.7013
Sr3-O1	(*4)	2.743(13)
Sr3-O2	(*4)	2.84(4)
Sr3-O4	(*4)	2.661(14)
<Sr3-O>		2.748

perovskites with 224 superstructure, for which charge or-

dering was suggested for Co1 (Co^{3+}) and Co2 (Co^{4+})^{9,18}. Using disordered A-cation positions the refined average <Sr/La-O> bond lengths were found very similar for all three A-sites ranging from 2.7013 to 2.7662 Å. These values are in very good agreement with those observed for other randomly substituted strontium/lanthanum cobaltites with the mixed A-site position^{6,8}. To confirm this structure model, that infers no A-site ordering, a part of the sample with oxygen deficiency $\delta=0.28$ was annealed under high-pressure oxygen at low temperatures (180 bar at 430°C, followed by slow cooling) in order to obtain fully oxygenated compound with $\delta=0$. The annealed sample showed single-phase x-ray diffraction pattern which could be indexed using simple cubic ($Pm-3m$) perovskite structure similar to that previously discussed for the $\delta=0$ sample obtained from 250 bar and 500°C. The absence of superlattice peaks confirmed mixed occupancy of the A-site by La and Sr for both samples with oxygen contents before ($\delta=0.28$) and after annealing ($\delta=0$). Our results suggest, that in contrast to other cobaltites with smaller rare earth elements $\text{Ln}_{1-x}\text{Sr}_x\text{CoO}_{3-\delta}$ ($x=0.67$ and 0.7) exhibiting the $a \approx 2a_p$ and $c \approx 4a_p$ superstructure, there is no Sr/La ordering in $\text{La}_{1/3}\text{Sr}_{2/3}\text{CoO}_{2.72}$. This observation allows us to exclude the role of A-site cation ordering in preferential ordering of oxygen vacancies on the O2 sites. Consequentially, oxygen vacancy ordering alone seems to be the main reason for occurrence of the com-

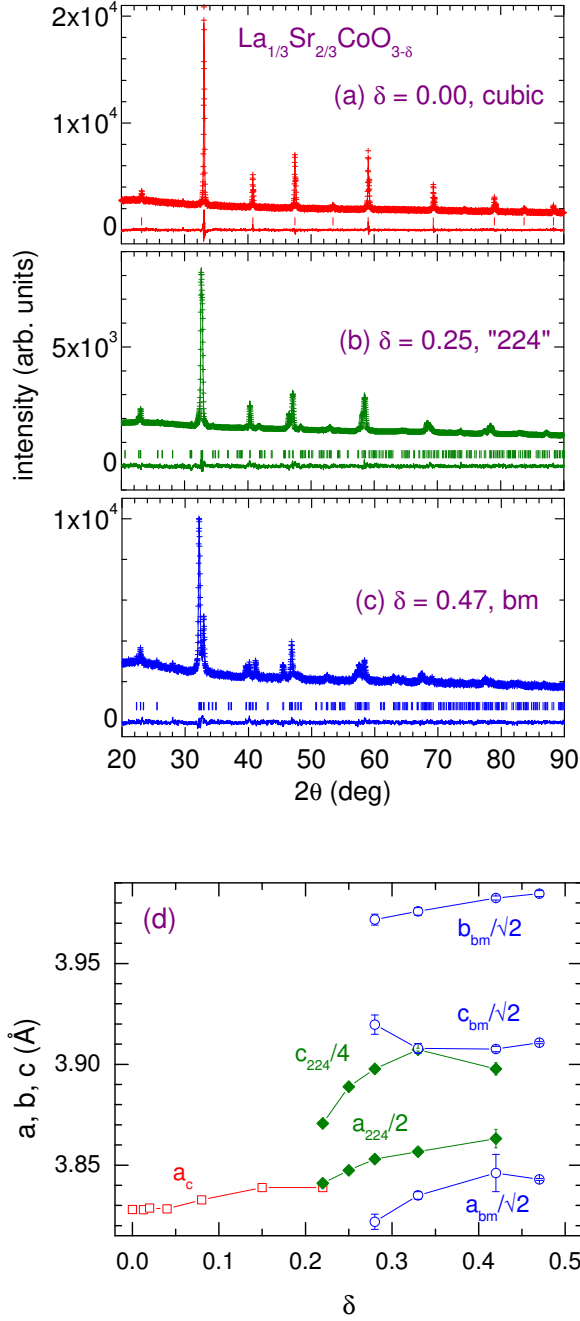


FIG. 1: (color online) (a-c) X-ray diffraction patterns for $\text{La}_{1/3}\text{Sr}_{2/3}\text{CoO}_{3-\delta}$ samples with different oxygen deficiencies δ . Experimental data points are presented as crosses. The continuous lines are the refined patterns and differences between the data and the refined patterns. Intensity peak positions are marked as short vertical lines. (d) Lattice parameters as a function of δ for three observed crystal structures: cubic (squares), “224” superstructure (diamonds), and brownmillerite (bm - circles) are presented.

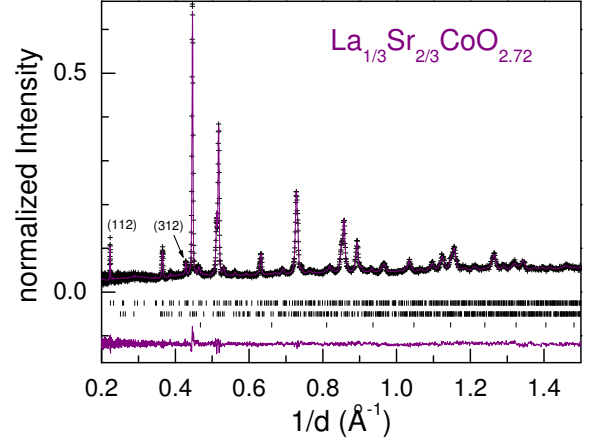


FIG. 2: (color online) Neutron diffraction pattern for $\text{La}_{1/3}\text{Sr}_{2/3}\text{CoO}_{2.72}$. Experimental data points are presented as crosses. The continuous lines are the refined patterns and differences between the data and the refined patterns. Intensity peak positions are marked as short vertical lines for the “224” superstructure, brownmillerite, and vanadium can (from top to bottom respectively).

plex “224” superstructure. Similar conclusions were recently made by S. Malo and A. Maignan²³ who observed the “224” superstructure for the $\text{SrTi}_{0.1}\text{Co}_{0.9}\text{O}_{3-\delta}$ compound with exclusively Sr^{2+} cations on the A-site. For highly doped cobaltites $\text{Ln}_{1-x}\text{A}_x\text{CoO}_{3-\delta}$ ($x \geq 0.5$, Ln = rare earth, A = alkaline earth) several perovskite-related superstructures have been reported. For example, the $a_p \times a_p \times 2a_p$ superstructure was proposed for $\text{La}_{0.3}\text{Sr}_{0.7}\text{CoO}_{2.82}$ ¹⁰, $\text{Ho}_{0.1}\text{Sr}_{0.9}\text{CoO}_{2.73}$ ²⁴ and for $\text{Ln}_{1-x}\text{Ba}_x\text{CoO}_{3-\delta}$ compounds.²⁵ Clearly, this superstructure model can not account for reflections observed in the NPD pattern of our sample and could not be used for $\text{La}_{1/3}\text{Sr}_{2/3}\text{CoO}_{2.72}$. The $\text{Ln}_{1-x}\text{Ba}_x\text{CoO}_{3-\delta}$ system revealed the $a_p \times 2a_p \times 2a_p$ and $3a_p \times 3a_p \times 2a_p$ superstructures arising from vacancy ordering in $[\text{LnO}_\delta]$ layer^{25,26}. Using these models with larger supercells we were not able to index all observed diffraction peaks in the NPD pattern for $\text{La}_{1/3}\text{Sr}_{2/3}\text{CoO}_{2.72}$. For example, reflections at $d = 1.78, 1.99, 2.33, 2.44, 4.47$ are not accounted in the $a_p \times 2a_p \times 2a_p$ model while reflections at $d = 2.33, 2.44, 4.47$ can not be indexed for the $3a_p \times 3a_p \times 2a_p$ superstructure. These peaks can be indexed only in the “224” superstructure [(312), (310), and (112), respectively].

C. Transport properties

Resistivity for several $\text{La}_{1/3}\text{Sr}_{2/3}\text{CoO}_{3-\delta}$ samples is presented in Fig. 3. The temperature dependence of resistivity shows metallic character for small oxygen deficiency ($0 \leq \delta \leq 0.08$). These samples are metallic below and above the Curie temperature T_C and show a weak

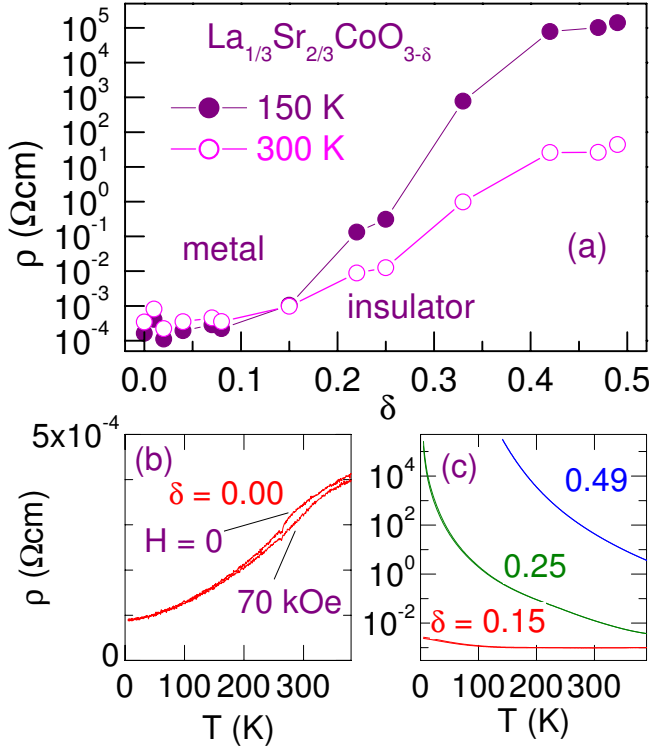


FIG. 3: (color online) (a) Resistivity at $T = 150$ and 300 K for $\text{La}_{1/3}\text{Sr}_{2/3}\text{CoO}_{3-\delta}$. (b),(c) Temperature dependencies of resistivity for selected values of δ .

negative magnetoresistance around T_C [see: Fig. 3(b)]. An insulating character is observed for both single-phase and mixed-phase samples with $0.22 \leq \delta \leq 0.49$ [Fig. 3(c)]. The crossover between these two types of behavior is observed for $\delta \approx 0.15$ at the boundary of the cubic perovskite structure [Fig. 3(a)]. It appears that the metal/insulator transition in $\text{La}_{1/3}\text{Sr}_{2/3}\text{CoO}_{3-\delta}$ is controlled by both the band filling (Co formal valence) and localization due to disorder (the oxygen vacancies δ). For stoichiometric $\text{La}_{1-x}\text{Sr}_x\text{CoO}_3$ samples, the metal/insulator transition was observed at strontium substitution of $x \approx 0.25$ in the rhombohedral structure.⁶ Since x in fully oxygenated $\text{La}_{1-x}\text{Sr}_x\text{CoO}_3$ is equal to the fraction of Co^{4+} ions, we can see that the metal/insulator transition (by changing the oxygen content) in $\text{La}_{1/3}\text{Sr}_{2/3}\text{CoO}_{3-\delta}$ takes place for significantly larger fraction of Co^{4+} ($\approx 37\%$, see: Table I) than for $\text{La}_{1-x}\text{Sr}_x\text{CoO}_3$ ($\approx 25\%$). That indicates that the insulating state is enhanced by the disorder already in the cubic structure for $\delta \approx 0.15$ and fully quenched in “224” and brownmillerite phases with Co formal valences ≈ 3.17 and ≈ 2.7 , respectively.

D. Magnetic properties

The ac susceptibility and dc magnetization for several $\text{La}_{1/3}\text{Sr}_{2/3}\text{CoO}_{3-\delta}$ samples are presented in Fig. 4(b)-

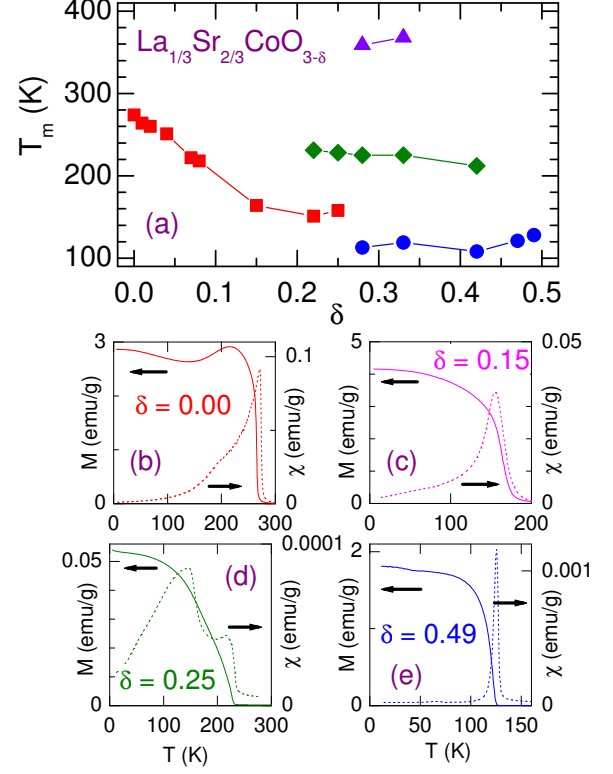


FIG. 4: (color online) (a) Magnetic transition temperatures for $\text{La}_{1/3}\text{Sr}_{2/3}\text{CoO}_{3-\delta}$. (b)-(e) Temperature dependencies of ac susceptibility (dashed lines, right axis) and dc magnetization (“field cooled” in 20 Oe, solid lines, left axis) for selected δ .

(e). The magnetic transition temperatures (T_m) were determined from the dc magnetization curves $M(T)$ (measured on cooling in the magnetic field of 20 Oe) as the temperatures of the maximum slope $-dM/dT$ [Fig. 4(a)]. These temperatures also coincide with the peaks of the ac susceptibility. The samples with cubic structure show ferromagnetic transitions with temperatures linearly decreasing from 274 to 160 K for δ increasing from 0 to 0.15. The “224” ($\delta \approx 0.25$) and brownmillerite ($\delta \approx 0.5$) phases show weak ferromagnetic transitions at 230 and 120 K, respectively. The samples that exhibit a mixture of two crystallographic phases also show two ferromagnetic transitions. Therefore, we can find a one-to-one correlation between the crystal structures and ferromagnetic phases in $\text{La}_{1/3}\text{Sr}_{2/3}\text{CoO}_{3-\delta}$ [Fig. 1(b) and Fig. 4(a)]. It is important to note that the two-phase nature of the samples is sometimes difficult to observe in magnetization measurements alone. On the other hand, the ac susceptibility shows clear two transitions for such samples.

The magnetization in the intermediate temperature range shows broad antiferromagnetic transitions for most of the samples, for which the $2a_p \times 2a_p \times 4a_p$ is the ma-

jority phase ($\delta = 0.28$ and 0.33). The transition temperatures for the $\delta = 0.28$ sample (studied with NPD) and the $\delta = 0.33$ sample are 359 and 368 K, respectively. The small change of magnetization at the transition temperature is typical of the G -type antiferromagnetic materials and usually is better visible in a higher magnetic field (10 kOe in this case).

The magnetization hysteresis curves for selected $\text{La}_{1/3}\text{Sr}_{2/3}\text{CoO}_{3-\delta}$ samples at $T = 5$ K are presented in Fig. 5(b)-(e). The high-field magnetization, determined from the magnetization curves, shows a clear saturation for $\delta \leq 0.15$. These samples demonstrate a typical ferromagnetic behavior. Therefore, we refer to the high-field magnetization as to the saturation magnetization. The magnetic transition temperatures are also equivalent to the ferromagnetic Curie temperatures ($T_m \equiv T_C$). The saturation magnetization linearly decreases in this range of δ [Fig. 5(a)]. For higher δ , the high-field magnetization drastically decreases and a linear contribution to the $M(H)$ curve is observed. These observations indicate a weak nature of ferromagnetism, probably associated with a canted antiferromagnetic state for “224” and brownmillerite phases. Future neutron diffraction experiments are expected to reveal the actual type of magnetic ordering at low temperatures in our samples.

The molar dc susceptibility $\chi_m = M/H$ in the temperature range 300-800 K was fitted to the general Curie-Weiss formula:

$$\chi_m = \chi_0 + (\mu_B N_A / 3k_B) \mu_{\text{eff}}^2 / (T - \Theta), \quad (1)$$

where χ_0 is a temperature-independent background susceptibility, N_A is the Avogadro constant, k_B is the Boltzmann constant, Θ is the paramagnetic Curie-Weiss temperature, μ_{eff} is the effective paramagnetic moment. For the samples with smaller $\delta < 0.15$ we used a narrower fitting range 300-500 K because of the oxygen loss from the samples above 500 K during the measurements in the magnetometer under a low pressure of helium gas. For the sample with $\delta = 0.33$, which showed the antiferromagnetic transition at 368 K, the fitting range 430-800 K was applied.

The characteristic temperatures T_m and Θ are presented in Fig. 6(a) for $\text{La}_{1/3}\text{Sr}_{2/3}\text{CoO}_{3-\delta}$. For small values of $\delta \leq 0.15$, Θ is positive and closely follows T_C . For each two-phase sample with $\delta = 0.22$ - 0.33 , Θ is also positive, which is a resultant value for the two coexisting phases. For $\delta = 0.47$ and 0.49 , Θ becomes negative, which indicates a dominating contribution of antiferromagnetic interactions between random cobalt spins in the paramagnetic state.

The analysis of the effective paramagnetic moment μ_{eff} along with the saturation magnetization M_{sat} provides us with information on the spin states of magnetic cobalt ions in $\text{La}_{1/3}\text{Sr}_{2/3}\text{CoO}_{3-\delta}$. Formal valence of cobalt in this material can be expressed as $(3+2/3-2\delta)+$, as listed in Table I.

It is worth noting that after increasing oxygen deficiency to $\delta > 1/3$, the formal Co valence is less than $3+$,

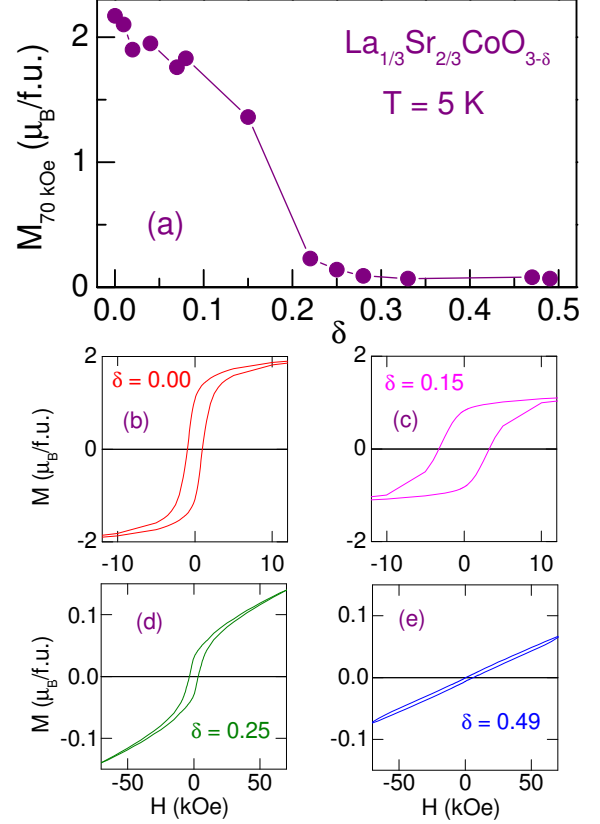


FIG. 5: (color online) (a) High-field magnetization in $H = 70$ kOe and $T = 5$ K for $\text{La}_{1/3}\text{Sr}_{2/3}\text{CoO}_{3-\delta}$. (b)-(e) Magnetization curves for several values of δ at 5 K.

which is unique to Sr substituted rare-earth cobaltites. In this case, a mixture of Co^{2+} and Co^{3+} ions results in dominating antiferromagnetic interactions and small spin canting with net weak ferromagnetic behavior. Large values of the effective paramagnetic moment in this oxygen content range suggest high-spin configuration of both Co^{2+} and Co^{3+} ions ($\text{Co}^{2+}\text{HS} + \text{Co}^{3+}\text{HS}$). This configuration has been found to satisfactorily describe the properties of $\text{Co}^{2+}/\text{Co}^{3+}$ containing $\text{LnBaCo}_2\text{O}_5$.²⁷

For $\delta = 1/3$ this formal valence of Co is equal to $3+$. For smaller δ we consider a mixture of Co^{3+} and Co^{4+} ions with the ratio $f_{3+}\text{Co}^{3+}:f_{4+}\text{Co}^{4+}$, where $f_{3+} = 1/3 + 2\delta$ and $f_{4+} = 2/3 - 2\delta$ are fractions of Co^{3+} and Co^{4+} , respectively. Assuming only ferromagnetic ordering of the cobalt ions, the saturation magnetization for this material can be described as $M_{\text{sat}} = 2f_{3+}S_{3+} + 2f_{4+}S_{4+}$, where S_{3+} and S_{4+} are spin states for Co^{3+} and Co^{4+} , respectively. Co ions can exhibit several possible spin states: low-spin t_{2g}^6 ($S_{3+} = 0$), intermediate-spin $t_{2g}^5e_g^1$ ($S_{3+} = 1$), and high-spin $t_{2g}^4e_g^2$ ($S_{3+} = 2$) for Co^{3+} and low-spin t_{2g}^5 ($S_{4+} = 1/2$), intermediate-spin $t_{2g}^4e_g^1$ ($S_{4+} = 3/2$), and high-spin $t_{2g}^3e_g^2$ ($S_{4+} = 5/2$) for Co^{4+} . Our high-field magnetization data, presented in Fig. 7(a)

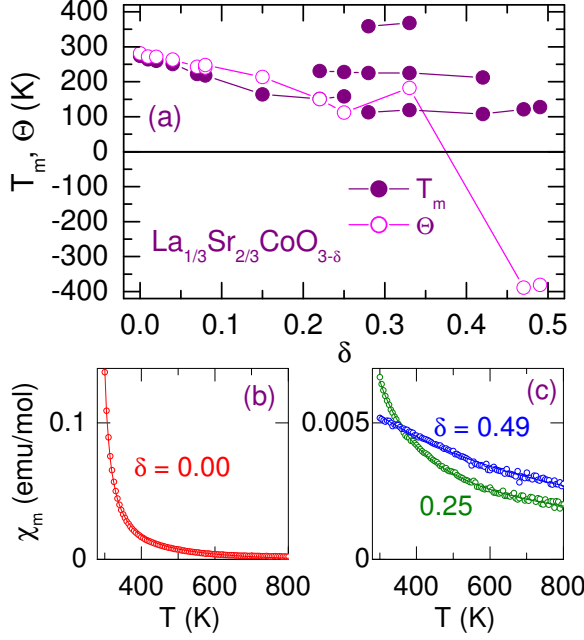


FIG. 6: (color online) (a) The magnetic transition temperatures T_m (filled circles) and Curie-Weiss temperatures Θ (open circles) for $\text{La}_{1/3}\text{Sr}_{2/3}\text{CoO}_{3-\delta}$. (b),(c) Molar susceptibility data for several values of δ , measured in $H = 1$ kOe. Lines are fits of the Curie-Weiss formula to the susceptibility data.

can be interpreted in the best way by assuming low-spin state for Co^{3+} and intermediate-spin state for Co^{4+} ($\text{Co}^{3+}\text{LS} + \text{Co}^{4+}\text{IS}$), which is illustrated in Fig. 7(a) as the dashed line. Only in this case, the low-spin Co^{3+} ions could account for a fast decrease of the saturation magnetization with δ in $\text{La}_{1/3}\text{Sr}_{2/3}\text{CoO}_{3-\delta}$. The combination of both Co^{3+} and Co^{4+} in the intermediate-spin state [$(\text{Co}^{3+}\text{IS} + \text{Co}^{4+}\text{IS})$: solid line in Fig. 7(a)] gives too high values of saturation magnetization.

The effective paramagnetic moment μ_{eff} is presented in Fig. 7(b). The spin-only value of the effective paramagnetic moment for $\delta < 1/3$ can be taken as $\mu_{\text{eff}}^2 = g^2[f_{3+}S_{3+}(S_{3+} + 1) + f_{4+}S_{4+}(S_{4+} + 1)]$, where $g = 2$ is the gyromagnetic factor. The μ_{eff} dependence on δ is illustrated in Fig. 7(b) as the dashed and solid line for combinations of $\text{Co}^{3+}\text{LS} + \text{Co}^{4+}\text{IS}$ and $\text{Co}^{3+}\text{IS} + \text{Co}^{4+}\text{IS}$, respectively. The latter model gives a better approximation to the μ_{eff} data. The real values of μ_{eff} are expected to be higher than the values given by the spin-only model implemented here, due to the spin-orbit interaction and a nonzero orbital momentum expected for Co^{4+} ions if they are not in the high-spin state. However, this effect was found to be rather small for other transition metal ions with similar d electron configurations.²⁸ Both M_{sat} and μ_{eff} can also be reduced by the itinerant character of a fraction of the ferromagnetically coupled electrons. This effect can be pronounced for $\delta < 0.15$ (in the metallic con-

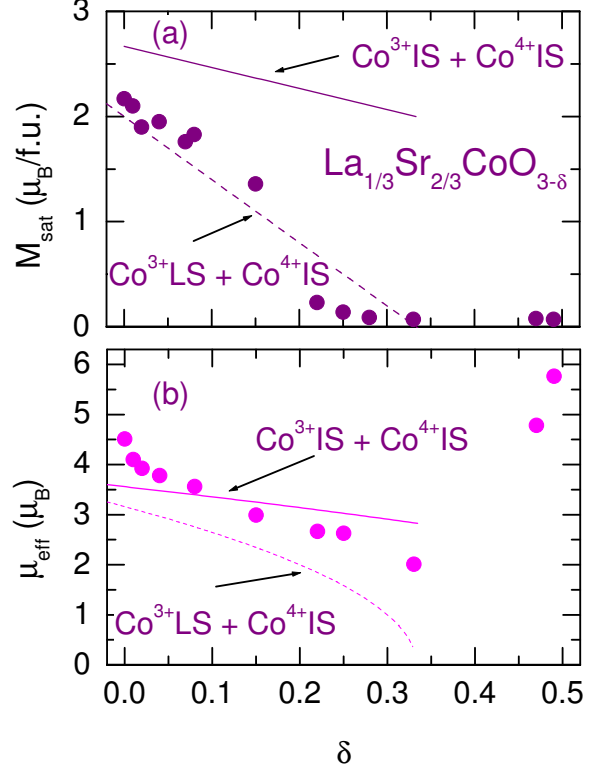


FIG. 7: (color online) (a) The magnetization in $H = 70$ kOe M_{sat} and (b) the effective paramagnetic moments μ_{eff} for $\text{La}_{1/3}\text{Sr}_{2/3}\text{CoO}_{3-\delta}$. Solid and dashed lines illustrate two models of spin states of Co ions (see: text).

ductivity range) but is expected to be less significant for larger $\delta > 0.15$, (above the metal-insulator transition). The observed different behavior between M_{sat} and μ_{eff} is equally striking for both metallic and insulating samples. The magnetic behavior of $\text{La}_{1/3}\text{Sr}_{2/3}\text{CoO}_{3-\delta}$ can be explained in a consistent way if we take into account a possible spin transition of Co^{3+} from low-spin to intermediate-spin state similar to LaCoO_3 .¹¹ In the light of this spin transition, the following spin-state combinations emerge: $\text{Co}^{3+}\text{LS} + \text{Co}^{4+}\text{IS}$ at $T \leq 5$ K and $\text{Co}^{3+}\text{IS} + \text{Co}^{4+}\text{IS}$ at temperatures above T_C .

IV. SUMMARY

In summary, we have synthesized a series of $\text{La}_{1/3}\text{Sr}_{2/3}\text{CoO}_{3-\delta}$ samples with precisely controlled $\delta = 0.00 - 0.49$. The samples show significant coupling among the structural, magnetic and transport properties as a function of δ . The stoichiometric material with $\delta = 0.00$ is a cubic ferromagnetic metal with the Curie temperature $T_C = 274$ K. The increase of δ to 0.15 is followed by a linear decrease of T_C to ≈ 160 K and a metal-insulator transition at the boundary of the cubic structure range.

Further increase of δ results in formation of tetragonal $2a_p \times 2a_p \times 4a_p$ phase for $\delta \approx 0.25$ and brownmillerite phase for $\delta \approx 0.5$. Those phases are weak ferromagnetic insulators (canted antiferromagnets) with magnetic transitions at $T_m = 230$ K and 120 K, respectively. The $2a_p \times 2a_p \times 4a_p$ phase is G -type antiferromagnetic between 230 K and ≈ 360 K. Magnetic properties of this system for $\delta < 1/3$ can be described in terms of a mixture of Co^{3+} ions in the low-spin state and Co^{4+} ions in the intermediate-spin state at low temperatures ($T \leq 5$ K) and both Co^{3+} and Co^{4+} ions in the intermediate-spin state at temperatures above T_C . For $\delta > 1/3$, the μ_{eff} data suggest a combination of Co^{2+} and Co^{3+} ions, both

in the high-spin state with dominating antiferromagnetic interactions.

Acknowledgments

This work was supported by NSF (DMR-0302617), the U.S. Department of Education, and the U.S. Department of Transportation. At ANL, this work was also supported by the U.S. Department of Energy, Division of Basic Energy Science-Materials Sciences, under Contract No. W-31-109-ENG-38 (the operation of IPNS).

-
- ¹ C. S. Tedmon Jr., H. S. Spacil, and S. P. Mitoff, J. Electrochem. Soc. **116**, 1170 (1969).
 - ² J. B. Goodenough and R. C. Raccach, J. Appl. Phys. **36**, 1031 (1965).
 - ³ A. V. Kovalevsky, V. V. Kharton, V. N. Tikhonovich, E. N. Naumovich, A. A. Tonoyan, O. P. Reut, and L. S. Boginsky, Mater. Sci. Eng. B **52**, 105 (1998).
 - ⁴ V. V. Kharton, A. A. Yaremchenko, A. V. Kovalevsky, A. P. Viskup, E. N. Naumovich, and P. F. Kerko, J. Membrane Sci. **163**, 307 (1999).
 - ⁵ H. L. Yakel, Acta Crystallogr. **8**, 394 (1955).
 - ⁶ A. Mineshige, M. Inaba, T. Yao, Z. Ogumi, K. Kikuchi, and M. Kawase, J. Solid State Chem. **121**, 423 (1996).
 - ⁷ M. A. Sen  r  s-Rodr  guez and J. B. Goodenough, J. Solid State Chem. **118**, 323 (1995).
 - ⁸ J. E. Sunstrom IV, K. V. Ramanujachary, M. Greenblatt, and M. Croft, J. Solid State Chem. **139**, 388 (1998).
 - ⁹ M. James, D. Casidy, D. J. Goossens, and R. L. Withers, J. Solid State Chem. **177**, 1886 (2004).
 - ¹⁰ R. H. E. van Doorn and A. J. Burggraaf, Solid State Ionics **128**, 65 (2000).
 - ¹¹ V. G. Bhide, D. S. Rajoria, G. Rama Rao, and C. N. R. Rao, Phys. Rev. **6**, 1021 (1972).
 - ¹² J. Wu and C. Leighton, Phys. Rev. B **67**, 174408 (2003).
 - ¹³ H. Taguchi, M. Shimada, and M. Koizumi, J. Solid State Chem. **29**, 221 (1979).
 - ¹⁴ P. Bezdzicka, A. Wattiaux, J. C. Grenier, M. Pouchard, and P. Hagenmuller, Z. Anorg. Allg. Chem. **619**, 7 (1993).
 - ¹⁵ J. D. Jorgensen, J. Faber Jr., J. M. Carpenter, R. K. Crawford, J. R. Haumann, R. L. Hittermann, R. Kleb, G. E. Ostrowski, F. J. Rotella, T. G. Worlton, J. Appl. Crystallogr. **22**, 321 (1989).
 - ¹⁶ A. C. Larson and R. B. von Dreele, *General Structure Analysis System*, Los Alamos Natl. Lab., LAUR 86-748, 1994; B. H. Toby, J. Appl. Cryst. **34**, 210 (2001).
 - ¹⁷ R. L. Withers, M. James, and D. J. Goossens, J. Solid State Chem. **174**, 198 (2003).
 - ¹⁸ D. J. Goossens, K. F. Wilson, M. James, A. J. Studer, and X. L. Wang, Phys. Rev. B **69**, 134411 (2004).
 - ¹⁹ D. J. Goossens, K. F. Wilson, and M. James, J. Phys. Chem. Solids **66**, 169 (2005).
 - ²⁰ S. Ya. Istomin, J. Grins, G. Svensson, O. A. Drozhzhin, V. L. Kozhevnikov, E. V. Antipov, and J. P. Attfield, Chem. Mater. **15**, 4012 (2003).
 - ²¹ S. Ya. Istomin, O. A. Drozhzhin, G. Svensson, E. V. Antipov, Solid State Sciences **6**, 539 (2004).
 - ²² E. O. Wollan and W. C. Koehler, Phys. Rev. **100**, 545 (1955).
 - ²³ S. Malo and A. Maignan, Inorg. Chem. **43**, 8169 (2004).
 - ²⁴ S. Streule, A. Podlesnyak, J. Mesot, K. Conder, N. Golosova, E. Mitberg, and S. Kazakov, Physica B **350**, e281 (2004).
 - ²⁵ A. Maignan, C. Martin, D. Pelloquin, N. Nguyen, and B. Raveau, J. Solid State Chem. **142**, 247 (1999).
 - ²⁶ W. S. Kim, E. O. Chi, H. S. Choi, N. H. Hur, S. - J. Oh, and H. C. Ri, Solid State Comm. **116**, 609 (2000).
 - ²⁷ E. Suard, F. Fauth, V. Caignaert, I. Mirebeau, and G. Baldinozzi, Phys. Rev. B **61**, R11871 (2000); F. Fauth, E. Suard, V. Caignaert, B. Domeng  s, I. Mirebeau, and L. Keller, Eur. Phys. J. B **21**, 163 (2001).
 - ²⁸ C. Kittel, *Introduction to Solid State Physics, Sixth Edition*, John Wiley & Sons, Inc. New York 1986.